Inference of Lightning Discharge-Element Orientation
from VHF Radio Polarimetry

Abram R. Jacobson[1,*], Robert H. Holzworth[1], Xuan_Min Shao[2], and Erin H. Lay[2]

1. University of Washington, Seattle, Washington, USA

2. Los Alamos National Laboratory, Los Alamos, New Mexico, USA

ABSTRACT:

We report an approach to infer lightning discharge-element orientation, using radio recordings on a satellite. The method must deal with the ionospheric distortion of the transionspheric radio signal, including magneto-ionic mode splitting.

INTRODUCTION

The spatio-temporal development of lightning leaders can be mapped within limited geographic areas in three dimensions by Very High Frequency (VHF) lightning mapper arrays, or LMAs [*Rison et al.*, 1999]. A one-dimensional (height) retrieval can be done, potentially globally, by time-resolving the ground reflection in satellite VHF recordings [*Jacobson et al.*, 1999; *Tierney et al.*, 2002]. It is reasonable to assume that a leader-step current element is aligned with the direction of discharge progress. However, some discharge events are either not immediately preceded, or not immediately followed, by temporal neighbors. In particular for such discharge events, an independent inference of channel orientation would be of great interest. We report preliminary work on a method to do this with satellite-based VHF recordings.

CONCEPT

The basic scheme for goniometry (angle determination) with two crossed antennas is shown in Figure 1. The signals from two crossed antennas (x and y) are syncronously and phase-coherently recorded. The time-varying electric field impinging on the antenna plane is assumed to be linearly polarized, along the red vectors. The point is to measure the relative amplitudes E_x and E_y, as well as the rotation angle θ. Each time that a new lightning-discharge element radiates a signal, a new determination of θ can be made on the new pulse. Figure 2 shows the geometry on the FORTE satellite. (a) Two log-periodic arrays, mutually orthogonal, are mounted on a nadir-directed boom extending ~ 10 m. (b) This shows the plane normal to the

---

∗ Contact information: Abram R. Jacobson, University of Washington, Seattle, Washington, USA, Email: abramj@u.washington.edu

boom and looking toward nadir. The y axis is along the ram direction, and θ is the angle of the electric-field axis y-ward from x.

Figure 3 shows a cartoon of a leader flash originating at the FI, the "flash initiation", and propagating upward toward a positive-charge region [*Rison et al.*, 1999; *Thomas et al.*, 2001], as is typical of normally (positive over negative) polarized clouds. The LMA provides the three-dimensional location of each detected spark, and hence the three-dimensional leader progression, from one node to the next, but not explicitly the angular orientation of a given dipole-radiator spark. Less capable than a ground-based LMA, VHF recordings from a single satellite can infer (at most) only one spatial dimension of discharge location, namely the discharge height (above ground), using the differential time of arrival between the direct and ground-reflected signals. The advantage however is that a satellite offers very broad geographic coverage. Figure 4 shows four examples of discharge height vs time, inferred from the ground-reflection time delay, during FORTE passes within sight of four different thunderstorms. The vertical strings of points are flashes with significant vertical extent, including leaders preceding ground-return strokes. This inference of height above ground is feasible for only those storms whose location is independently known, e.g. by a ground-based array such as WWLLN. It is also possible- though at this point in time not demonstrated to be practical -that the second view of an elevated (e.g, intracloud) emission emitter could be combined with the direct view to provide a stereoscopic reconstruction of the dipole orientation in *three* dimensions. See Figure 5.

EXAMPLE

We will illustrate our approach with paired, two-channel data in the FORTE "low band", 26-51 MHz, in which output from two receivers ("A" and "B") are each sampled at 50 megasamples/sec. The sample duration is 20480 samples, or about 400 microsec. The receivers frequency-shift the signal to baseband, so that 26 MHz at the input looks like DC at the output, etc. The sampling is exactly syncronous and coherent between the two channels, and the receivers are fed separate signals from the two orthogonal LPA's ("x" and "y"; see Figure 2 above). All of the steps to follow are automatically implemented and require no human interaction. Figure 6 shows raw spectrograms of the two-channel data, triggered (with 25% pretrigger in the record) by a broadband impulse from lightning at approximately 100 microsec. The impulse is dispersed with a dispersive delay approximately proportional to N_e/f^2, where N_e is the line-of-sight total electron content ("TEC"), and f is the wave frequency [*Roussel-Dupré et al.*, 2001].

Figure 6 indicates the presence not only of the main lightning-generated impulse, but also diffuse

broadband noise (also lightning-generated) as well as powerful narrow-band, man-made interference near 27 MHz. Since we wish to analyze the behavior of the main lightning impulse only, with minimal confusion from either the diffuse noise or the interference, we now perform an auto-clean of the data to isolate the main impulse. Figure 7 shows spectrograms of the two antennas' signals ("x" and "y"), *after dechirping and interference suppression* via spectral prewhitening [*Jacobson et al.*, 1999]. Figure 7(a,b) shows the dechirped signal with the dechirp optimized for the fast magneto-ionic mode, while Figure 7(c,d) is optimized for the slow magneto-ionic mode [*Massey et al.*, 1998; *Roussel-Dupré et al.*, 2001]. We emphasize that the spectrogram displays are based only on the spectral density, and ignore the phase. However, the underlying dechirped time-domain signals contain all the information including the phase. For the time-domain signal optimally dechirped for the fast mode (corresponding to the spectrograms in Figure 7a,b) we can remove the diffuse noise to the left of the fast mode by zeroing the time-domain data prior to the rise of the fast mode. Likewise, for the time-domain signal optimally dechirped for the slow mode (corresponding to the spectrograms in Figure 7c,d), we can remove the diffuse noise to the right of the slow mode by zeroing the time-domain data following the fall of the slow mode. This removes the vast majority of the diffuse, lightning-generated noise, leaving only the limited interstitial gap between the fast and slow modes, which is not accessible with this auto-clean procedure.

Following the auto-clean, the full natural dispersion of the cleaned signal is restored, and the processing then derives the Hilbert envelope of the dispersed clean signal. The amplitude of that envelope is shown in Figure 8 for (a) antenna x and (b) antenna y. The oscillation is the familiar Faraday beat, as the signal, whose Faraday rotation depends on frequency in such a manner as to appear to precess at a constant rate in the dispersed signal, alternates between alignment and orthogonality with respect to an antenna axis [*Jacobson and Shao*, 2001; *Massey et al.*, 1998]. The Faraday beat frequency is twice the Faraday precession frequency. Were the signal ideal, i.e. dispersed ideally according to N_e/f^2, split into magneto-ionic modes of equal amplitude, then the Faraday beat would show full amplitude extinction at the nulls. That this does not quite happen is a reminder that the signal is not fully ideal. In this example, the main non-ideal factor is that the slow mode is somewhat weaker than the fast mode. This causes the Hilbert "nulls" to fill in; in other words, the observed Faraday beat is not quite perfect-contrast.

The clean, naturally dispersed time-domain signal from antenna x is shown as the blue curve in Figure 9, bounded between the Hilbert envelope (solid black curve) and the negative of the Hilbert envelope (dashed black curve). This is to be compared with the theoretical expectation for the time-domain impulse-response functions S_x and S_y [*Massey et al.*, 1998]:

$$S_x(t) \propto$$

$$\left\{\frac{1}{(\alpha N_e(t-t_0))^{\frac{3}{4}}}\right\} X \left\{\cos(\theta_0 + \omega_{ce}\cos(\beta)(t-t_0))\right\} X \left\{\cos\left(4\pi(\alpha N_e(t-t_0))^{\frac{1}{2}}\right)\right\} \quad (1)$$

$$S_y(t) \propto$$

$$\left\{\frac{1}{(\alpha N_e(t-t_0))^{\frac{3}{4}}}\right\} X \left\{\sin(\theta_0 + \omega_{ce}\cos(\beta)(t-t_0))\right\} X \left\{\cos\left(4\pi(\alpha N_e(t-t_0))^{\frac{1}{2}}\right)\right\} \quad (2)$$

The time t_0 in Eqs. (1, 2) is the time-of-arrival in the absence of dispersion, i.e. at "infinite frequency". The symbol β is the angle between the wavevector **k** and the geomagnetic field **B** while the symbol ω_{ce} is the electron angular gyrofrequency. With time in units of microsec and N_e in units of 10^{17} m^{-2}, the constant α is approximately 1.34 [*Massey et al.*, 1998]. The impulse response function is the product of three factors, each in curly brackets. The first factor is a slow amplitude modulation of the dispersed signal, and is the factor least evident in the data (Figure 9). The first factor is expected to be the same for both antennas. The second factor is the Hilbert envelope of the dispersed signal, in quadrature between the two antennas. The Hilbert envelope varies due to the time-dependency of the Faraday angle θ, given by

$$\theta = \theta_0 + \omega_{ce}\cos(\beta)(t-t_0) \quad (3)$$

Note that θ_0 is the starting angle of the Faraday precession, and is the goniometric angle we seek. The third factor in the impulse response is the pure dispersed time-domain carrier, without the magneto-ionic effect. This factor is expected to be the same for the two orthogonal antennas.

The analysis procedure now takes the cleaned, dispersed signal (blue curve in Figure 9 above) and fits amplitude, Hilbert precession, and carrier factors. The amplitude is treated as purely a slow, empirical variation, and is not forced to fit the form of the first factor in the theoretical impulse response. However, the Hilbert precession is fitted to the cosine (for antenna x) or sine (for antenna y) of the precession angle given by Eq. (3), while the carrier factor is fitted to the common last factor in the impulse response. We reiterate that this fit involves four adjustable parameters: t_0, N_e, $\omega_{ce}\cos(\beta)$, and θ_0. Only three are truly independent; the goniometric phase θ_0

follows directly from the other three. The fit of the impulse response to the data does match the observations quite nicely, as seen in Figure 10, examining the x-antenna signal. Two short segments are show, the first (a) between 2-6 microsec, and the second (b) between 9-13 microsec. The blue curve is the observed data, the red curve is the overall fit, and the black curves are the Hilbert envelope (solid) and the negative of the Hilbert envelope (dashed). The best-fit Hilbert envelope is sinusoidal, so that its amplitude has true nulls, unlike the data.

Figure 11 shows the correlation of the best-fit model with the actual data from the x-antenna signal, as a function of two of the fitting parameters: TEC on the horizontal axis, and time-of-arrival at infinite frequency on the vertical axis. The heavy red polyon is centered on the global optimum. There are multiple false optima, and the overall elongation of the region of variation indicates a moderate degree of parameter degeneracy between the two axes.

Figure 12 shows details on the Hilbert-envelope phase θ (see Eq. 3). Figure 12(a) shows the Hilbert phase in the data (black curve). We fit a second-order polynomial to this variation. The zeroth- and first-order terms of this fit together provide the blue straight line in Figure 12(a). There is a noticeable residual error between this straight line and the data. Figure 12(b) shows that residual (black curve) as well as the fitted parabola, which adequately fits the residual. The residual vanishes at $t = 0$, and grows quadratically at later times (see discussion of why, below).

This indicates that prior to $t = 0$, the straight-line fit alone suffices to our needed level of precision. Figure 13 shows both the data (black curve) and a straight-line extrapolation (green) back to $t = t_0$ (red vertical line). The intersection of the green extrapolation with the red line indicates the starting phase θ_0 (plus integer multiples of 2π), which is the sought goniometric angle.

The residual (black curve) in Figure 12b, which is well fitted by the parabolic term (red curve), is probably related to slight raybending effects, which are expected to grow at the lowest frequencies [*Roussel-Dupré et al.*, 2001]. Figure 14 illustrates how this happens [*Jacobson and Shao*, 2001]. We had assumed that the angle β between **k** and **B** is constant for all frequencies in the band, but this is slightly spoiled by raybending. Figure 14 is a cartoon of a spherical-shell ionosphere, with refractive bending occuring at two Snell's Law interfaces between the emitter ("e") and the satellite. The example considered here is one in which the raypath is less inclined (off of horizontal) than is the Earth's magnetic field. Since the index of refraction in the ionosphere exceeds unity for this frequency regime, the raybending acts to increase the angle β more toward orthogonality between **k** and **B**. This reduces the Faraday angular precession rate

$\omega_{ce}\cos(\beta)$ more for low frequencies than for high frequencies. In terms of the dispersed time-domain signal (Figure 9 above), raybending causes a reduction of the precession rate vs time during the dispersed pulse. That is the origin of the slight weakening of the slope of phase-vs-time in the data (black curve in Figures 12a and 13).

Using the extrapolated Hilbert-envelope phase from Figure 13, we show in Figure 15 the extrapolation of the Hilbert envelope itself for antenna x's signal. The green curve is the extrapolation back to $t = t_0$, the red vertical line marks $t = t_0$, the black curve is the observed Hilbert envelope, and the blue curve is the envelope modeled with only the straight-line fit to the phase.

ASSESSMENT AND OUTLOOK

Although the forgoing example suggests a very tidy solution for the fitted parameters t_0, N_e, $\omega_{ce}\cos(\beta)$, and θ_0, we suspect that systematic errors in the determination of t_0 will lead to an unacceptably large error in the goniometric angle θ_0. Those two parameters are highly correlated. Note that the Hilbert precession period is about 2 microsec, so that the Faraday beat period is about 1 microsec. The Faraday beat period (null-to-null) corresponds to evolution of the angle θ through 180 deg. Suppose we seek an accuracy of one-twentieth of this, namely 9 deg, in the derivation of the goniometric angle θ_0. This implies that we must retrieve t_0 with an accuracy of 50 nanosec. We have demonstrated in the forgoing example what can be accomplished with practical "polarimetric" data from FORTE, in which both synronously-sampled receivers are tuned to the same passband and differ only in the antenna from which they derive their signal. Unfortunately, the polarimetric arrangement, with both receivers at the "low band" (26-51 MHz), probably does not have the skill to achieve 50-nanosecond accuracy in t_0, when we take account of the refractive perturbations of higher order [*Roussel-Dupré et al.*, 2001] than treated here. Moreover, it is not a help to use a higher frequency band on both antennas, despite the more straightforward retrieval of t_0, because at higher frequencies the duration of the dispersed signal is reduced, weakening the measurement of $\omega_{ce}\cos(\beta)$.

Both receivers at "low band" is the appropriate FORTE operational mode for deriving the polarimetric parameters of various signal components in the data [*Shao and Jacobson*, 2001; 2002]. At the outset of the present work on goniometry of source dipole emitters, it struck us as obvious that we should use the same operational mode as for polarimetry, for classic radio goniometry involves two crossed antennas, and we need sufficient dispersed signal duration to measure $\omega_{ce}\cos(\beta)$ with precision. However, we now realize that *two antennas are not needed to*

derive the goniometric angle θ_0. Because the signal vector precesses in the x,y plane, as long as we can accurately fit the phase of the progression angle vs time, then we need only one antenna at low band (26-51 MHz) to derive θ_0 in terms of t_0, the infinite-frequency arrival time. Fortunately, besides the polarimetric mode of FORTE operation, the other main mode was "mixed", with one receiver at low band, and the other at "high band" (118-143 MHz). This higher-frequency signal recording will in most circumstances allow us to estimate t_0, the infinite-frequency arrival time, with 50-nanosec absolute accuracy. In effect, the single antenna receiving the low-band signal "sees" the electric-field vector undergoing the Faraday beat. As long as the frequency of that beat can be determined, and as long as the zero-crossing phase can be determined, then the goniometric angle can be scaled from the infinite-frequency arrival time. This is illustrated in Figure 16. This two-band approach will be performed and tested by the time of the conference, and results will be presented in our poster.

REFERENCES

Jacobson, A. R., S. O. Knox, R. Franz, and D. C. Enemark (1999), FORTE observations of lightning radio-frequency signatures: Capabilities and basic results, *Radio Sci., 34*(2), 337-354.

Jacobson, A. R., and X.-M. Shao (2001), Using geomagnetic birefringence to locate sources of impulsive, terrestrial VHF signals detected by satellites on orbit, *Radio Sci., 36*(4), 671-680.

Massey, R. S., S. O. Knox, R. C. Franz, D. N. Holden, and C. T. Rhodes (1998), Measurements of transionospheric radio propagation parameters using the FORTE satellite, *Radio Sci., 33*(6), 1739-1753.

Rison, W., R. J. Thomas, P. R. Krehbiel, T. Hamlin, and J. Harlin (1999), A GPS-based three-dimensional lightning mapping system: Initial observations in central New Mexico, *Geophys. Res. Lett., 26*, 3573-3576.

Roussel-Dupré, R. A., A. R. Jacobson, and L. A. Triplett (2001), Analysis of FORTE data to extract ionospheric parameters, *Radio Sci., 36*(6), 1615-1630.

Shao, X.-M., and A. R. Jacobson (2001), Polarization observations of broadband VHF signals by the FORTE satellite, *Radio Sci., 36*(6), 1573-1589.

Shao, X.-M., and A. R. Jacobson (2002), Polarization observations of lightning-produced VHF

emissions by the FORTE satellite, *J. Geophys. Res.*, *107*(D20), 4430, doi:10.1029/2001JD001018.

Thomas, R. J., P. R. Krehbiel, W. Rison, T. Hamlin, J. Harlin, and D. Shown (2001), Observations of VHF source powers radiated by lightning, *Geophys. Res. Lett.*, *28*(1), 143-146.

Tierney, H. E., A. R. Jacobson, R. Roussel-Dupré, and W. H. Beasley (2002), Transionospheric pulse pairs originating in marine, continental and coastal thunderstorms: Pulse energy ratios, *Radio Sci.*, *37*(3), 10.1029/2001RS002506, doi:10.1029/2001RS002506.
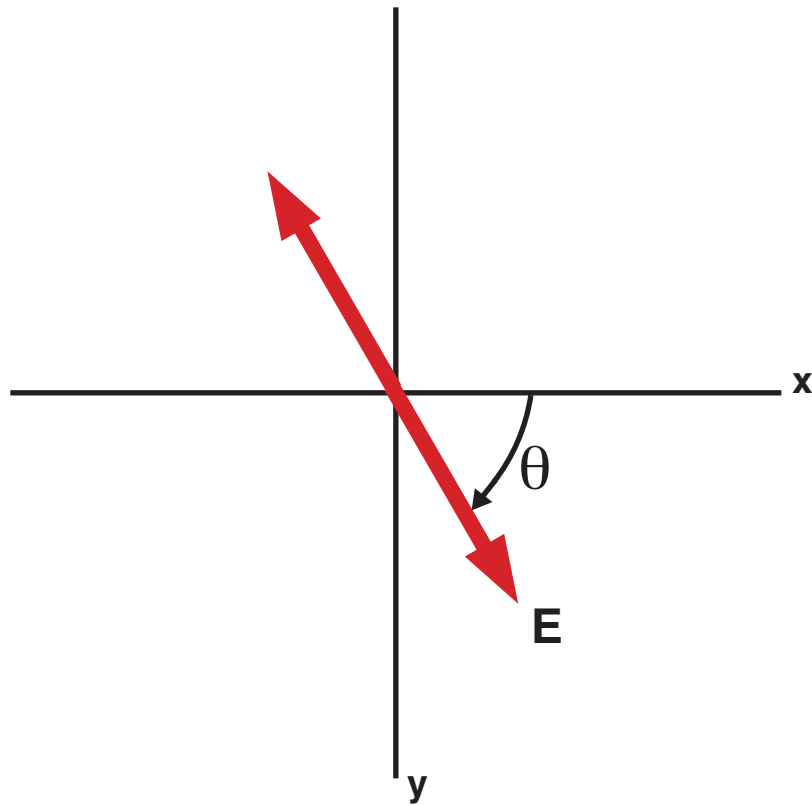
Figure 1: Cartoon of goniometric determination of an angle in the x, y plane. This is the plane containing two linearly-polarized antennas, one along each axis. The relative-phase and magnitude relationships between signals from the two antennas give the orientation of the electric field in the plane.

(a) nadir-directed LPAs

(b) projection onto xy plane normal to nadir, looking down

ram direction

Earth limb

Y

#2

left side

#1   X

right side

$-\theta$

E

anti-ram direction
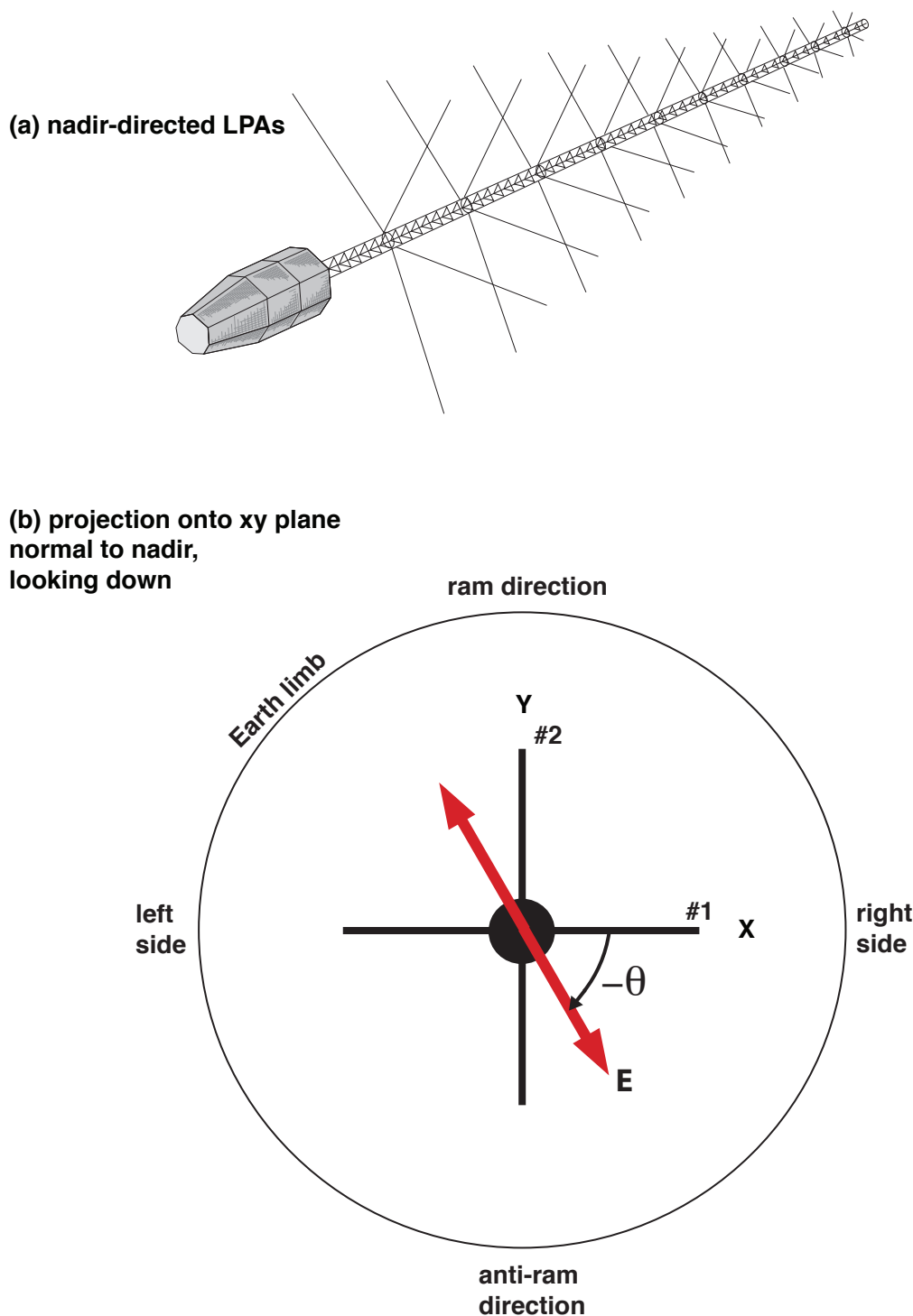
Figure 2: Implementation of angle measurement with FORTE radio antennas. (a) 10-m boom toward nadir holds two orthogonal log-periodic antennas (LPAs). (b) View of x, y plane normal to boom, looking down along nadir, showing goniometric determination of orientation of electric field's projection into the x, y plane.
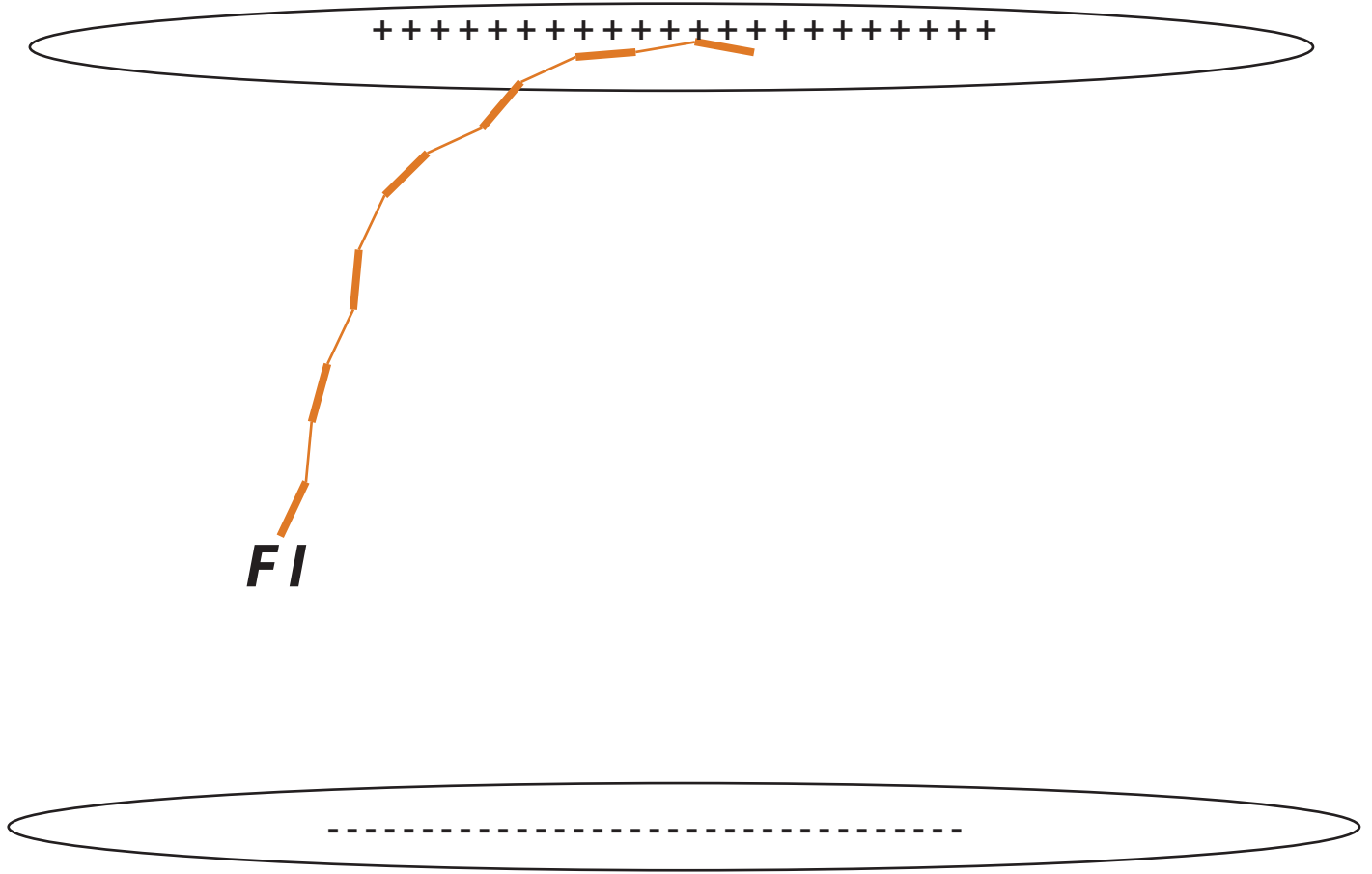
Figure 3: Cartoon of ascending intracloud leader, from the flash initiation (FI) upward and into the positive-charge region. The leader consists of successive quasi-discrete step segments, each of which behaves as a transient radiating dipole at the moment it is invested with charge.
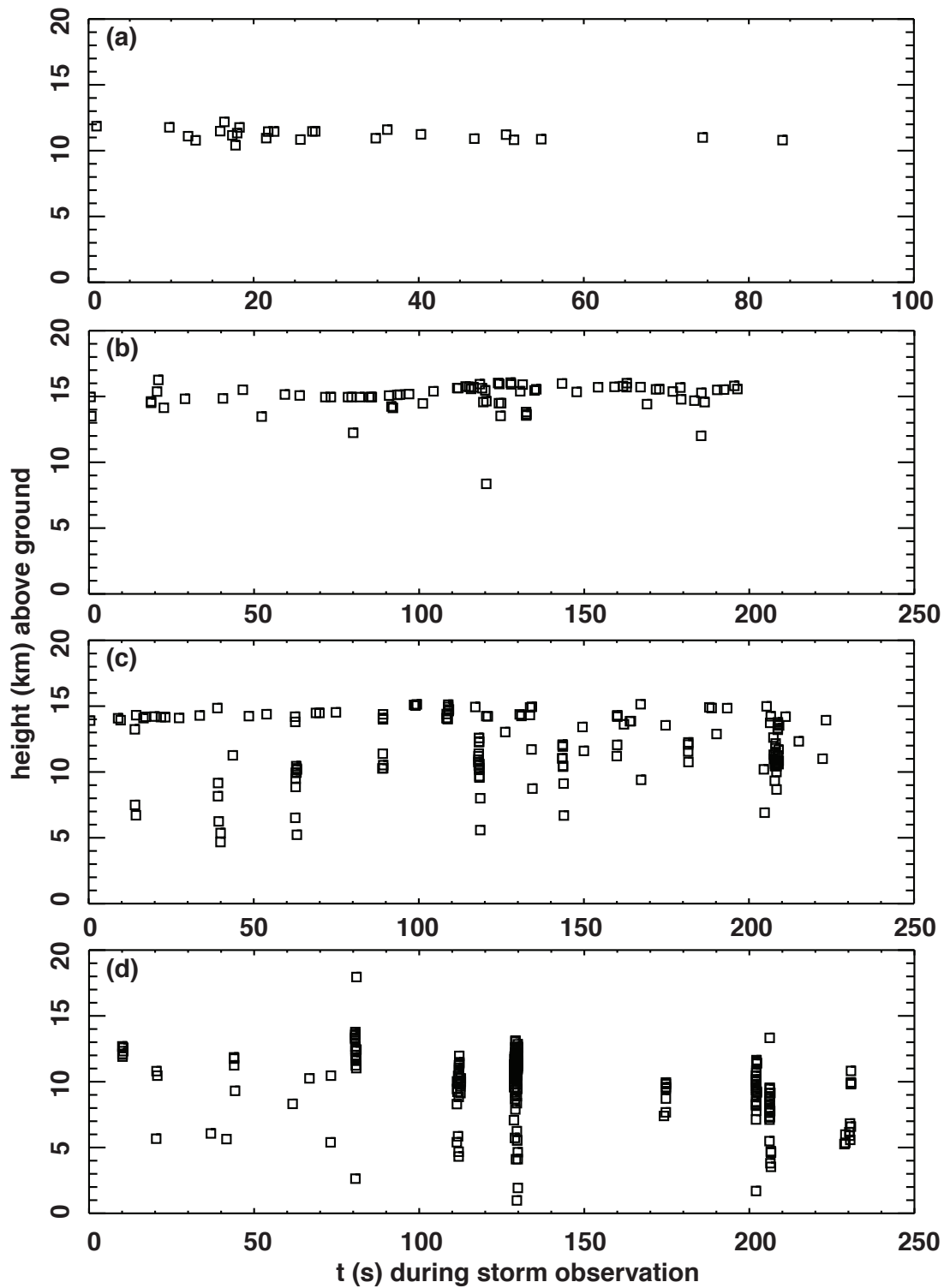
Figure 4: Four examples of discharge height vs time during FORTE passes within sight of thunderstorms. The height can be inferred for pulsed emission sources if the storms are geolocated by other means, e.g. ground-based VLF lightning-location arrays. Some of the leaders (lower panel) extend down to ground.
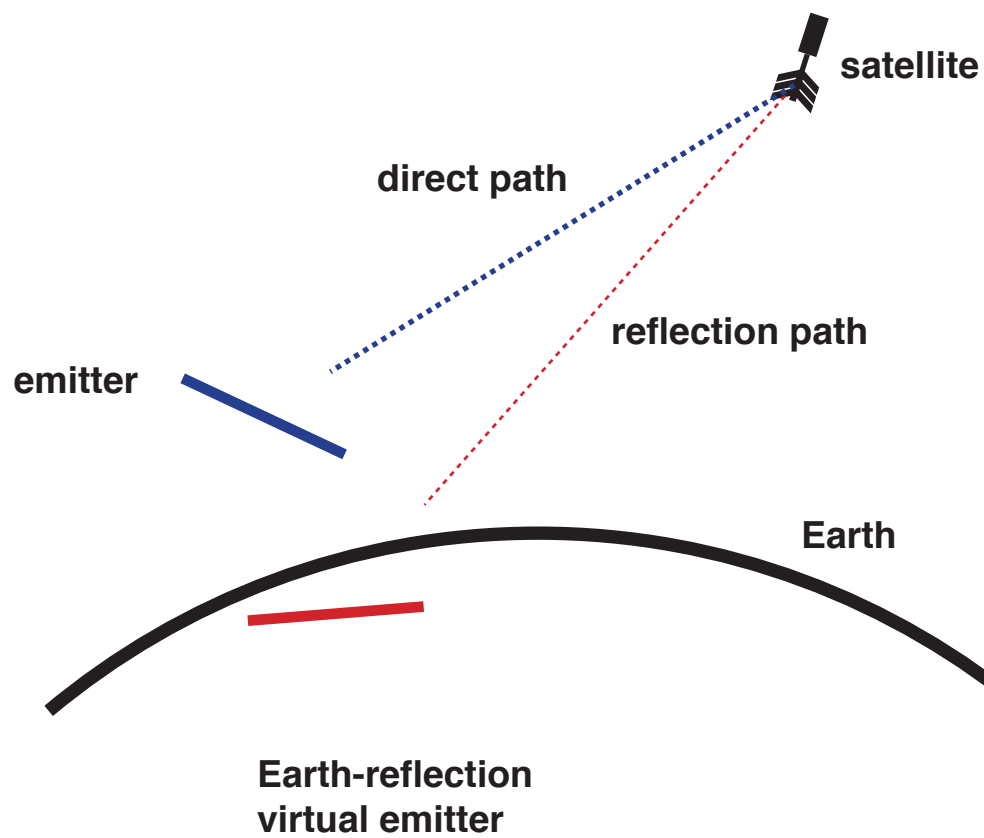
Figure 5: Cartoon of stereoscopic view of an elevated emitter, with direct and ground-reflected radio paths affording two different views of the emitter by the satellite.

file= f19980801_233850.das, event # 155
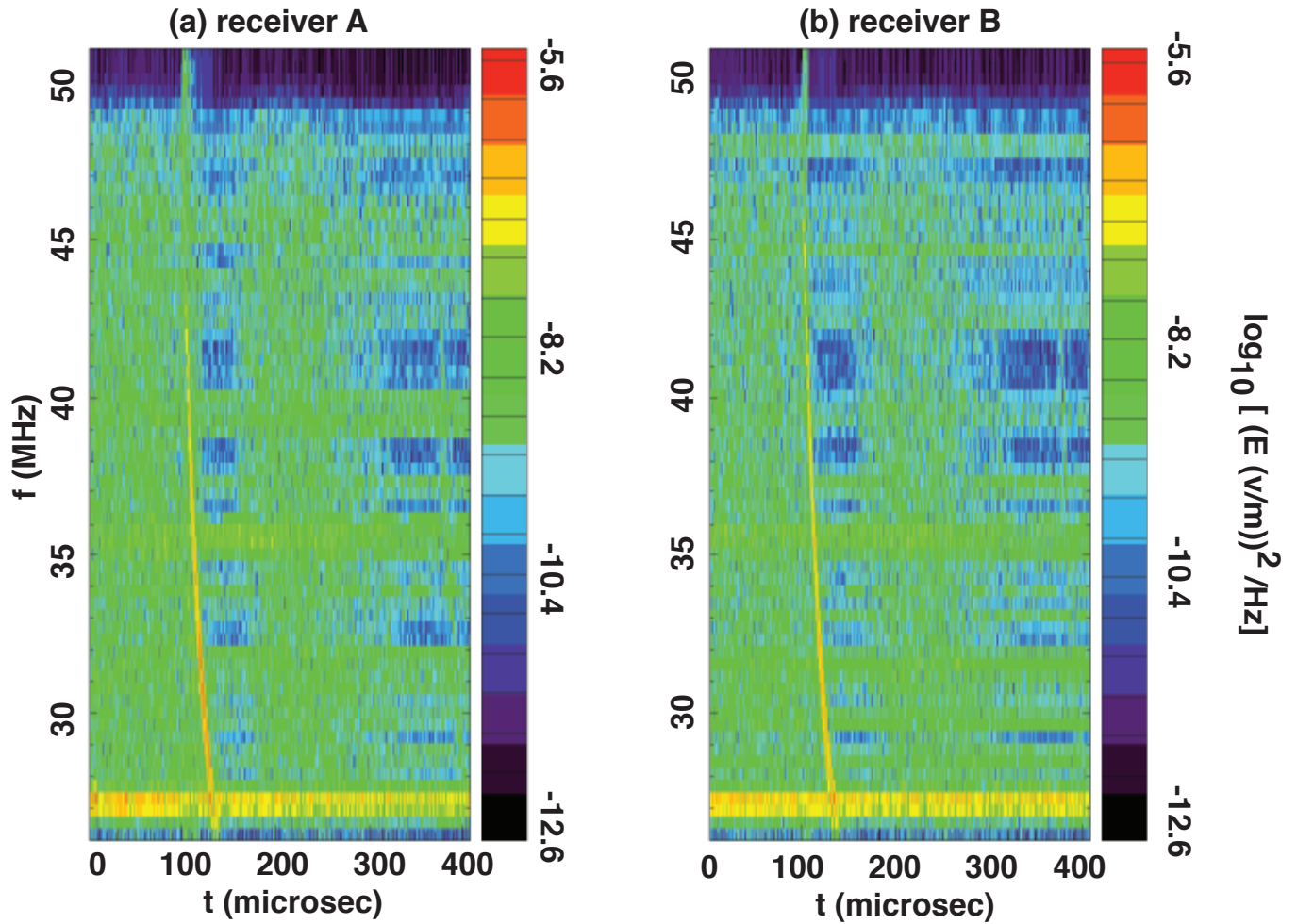
Figure 6: Raw spectrograms of the electric fields recorded by recievers of the two FORTE antennas, in the "low band" 26-51 MHz.

file= f19980801_233850.das, event # 155
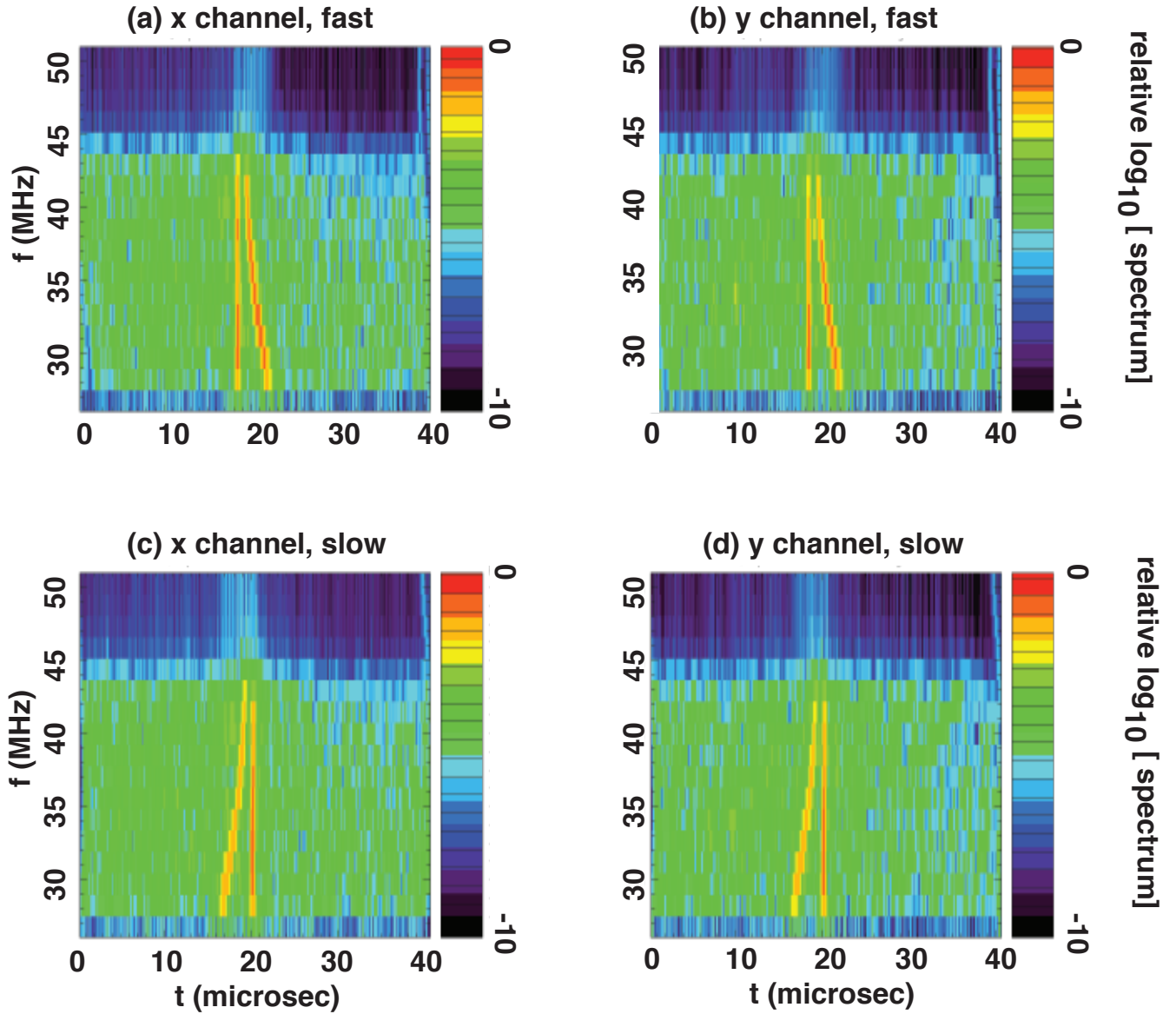
Figure 7: Detailed spectrograms of the electric fields along (a, c) the x antenna and (b, d) the y antenna. The two modes in each spectrogram are from the successive arrivals of the fast and slow magneto-ionic propagation modes. The purpose of dechirping is to optimally compress a pulse feature, i.e. remove its spectral dispersion. The electric field has been dechirped with either the fast-mode optimization (a, b) or the slow-mode optimization (c, d).

file= f19980801_233850.das, event # 155
(a) X-channel Hilbert amplitude

(b) Y-channel Hilbert amplitude
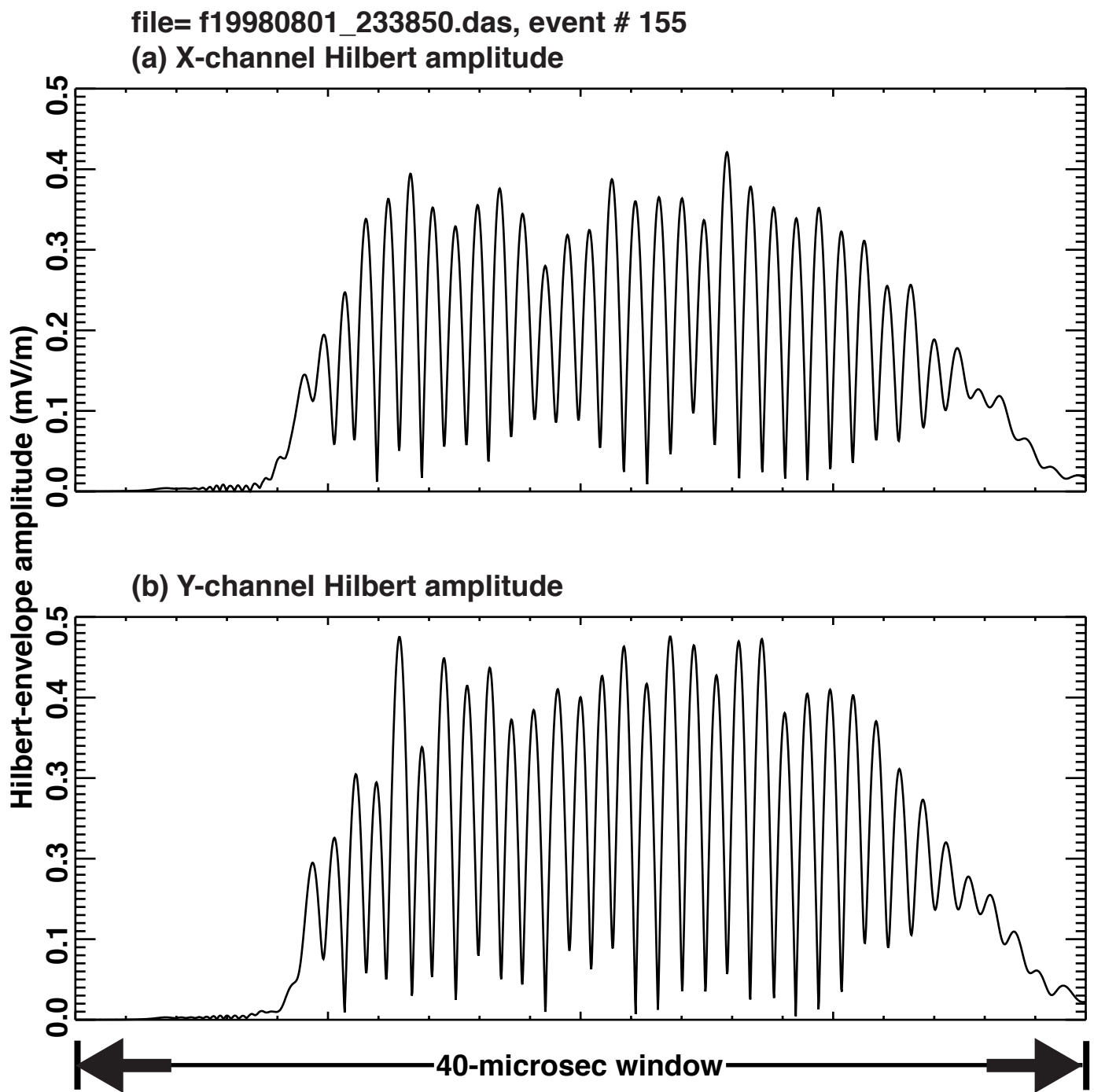
Figure 8: Positive-definite amplitude of the Hilbert envelope during a 40-microsec window containing the dispersed pulse.

file= f19980801_233850.das, event # 155
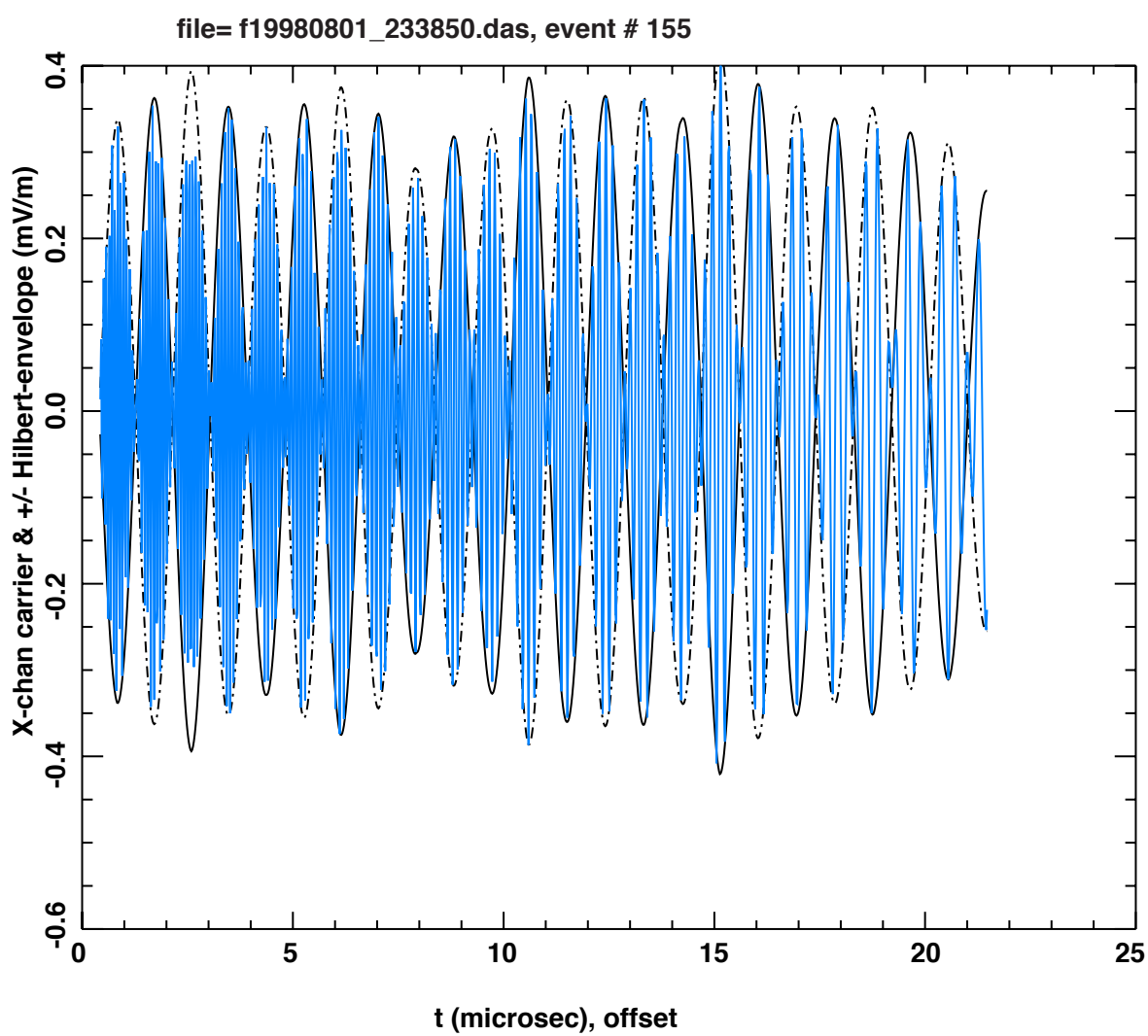
Figure 9: Full signal (blue curve) with plus and minus the Hilbert envelope (solid and dashed black curves), for antenna x.
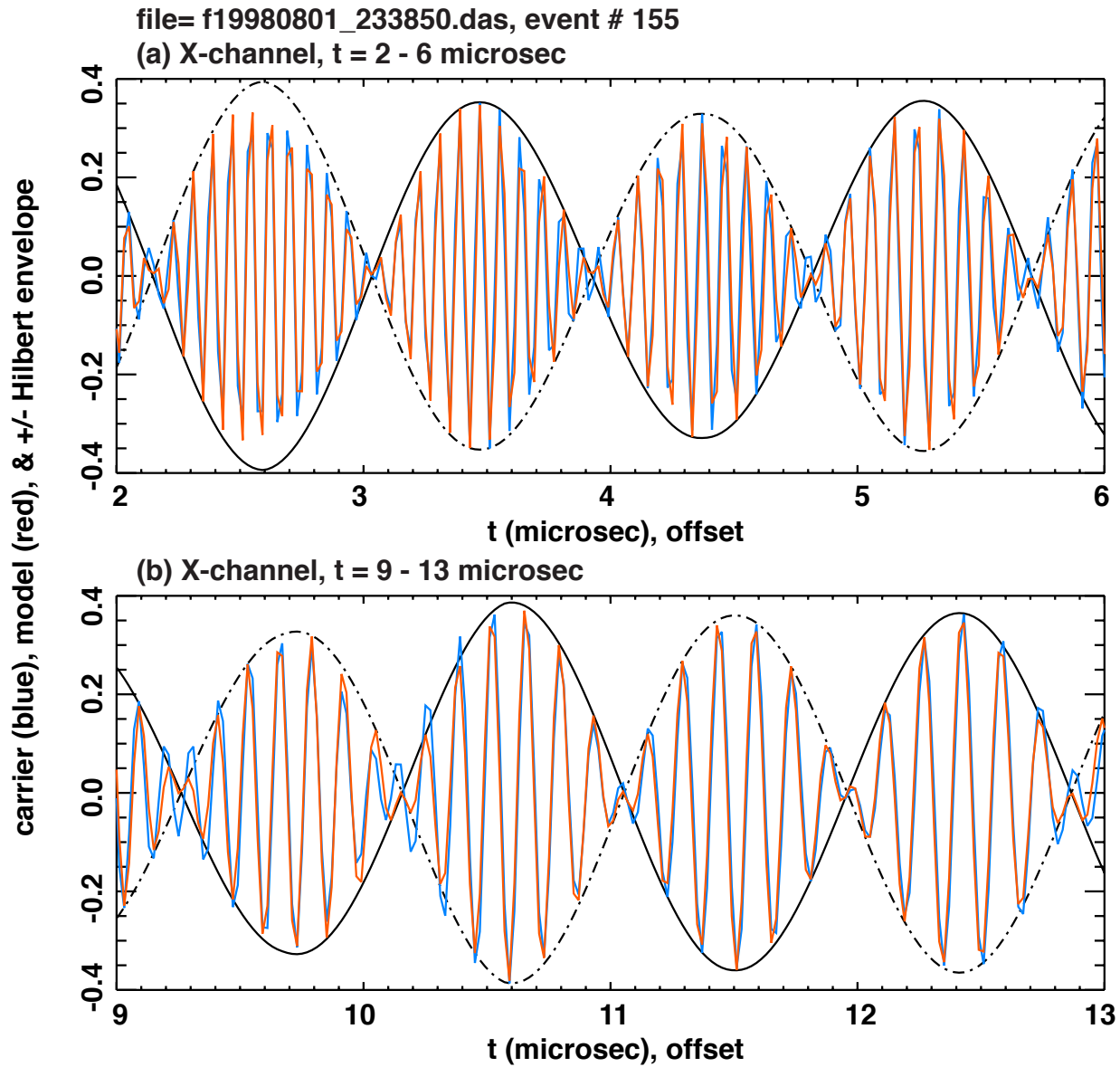
Figure 10: Zoom view of two four-microsec segments of the signal on the x antenna. Blue: data. Red: model of recorded signal. Black: plus (solid) and minus (dashed) Hilbert envelopes
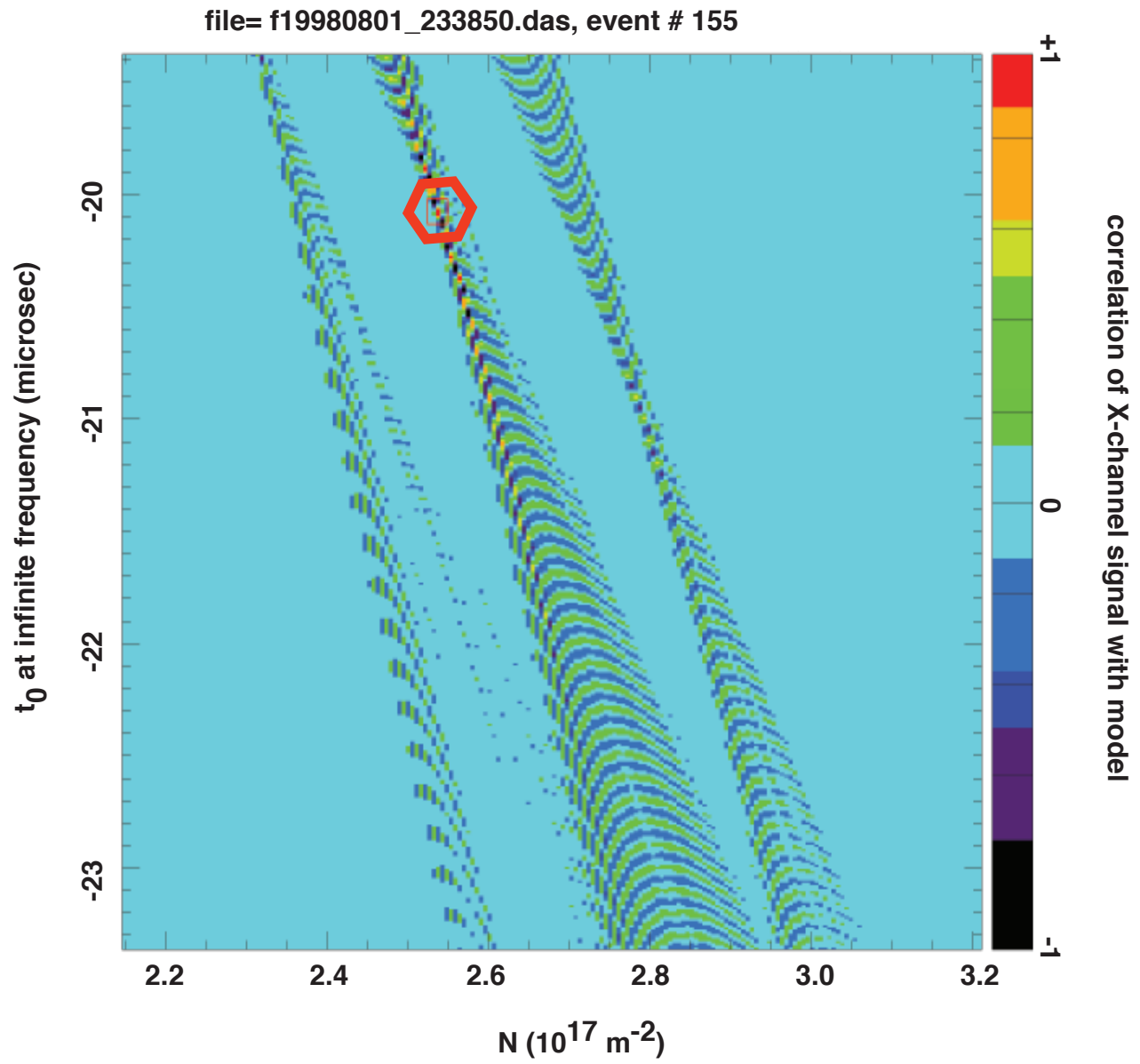
Figure 11: Correlation between data and model waveforms for the x antenna, versus line-of-sight TEC (horizontal) and time-of-arrival at infinite frequency (vertical). The large red polygon surrounds the global optimum.
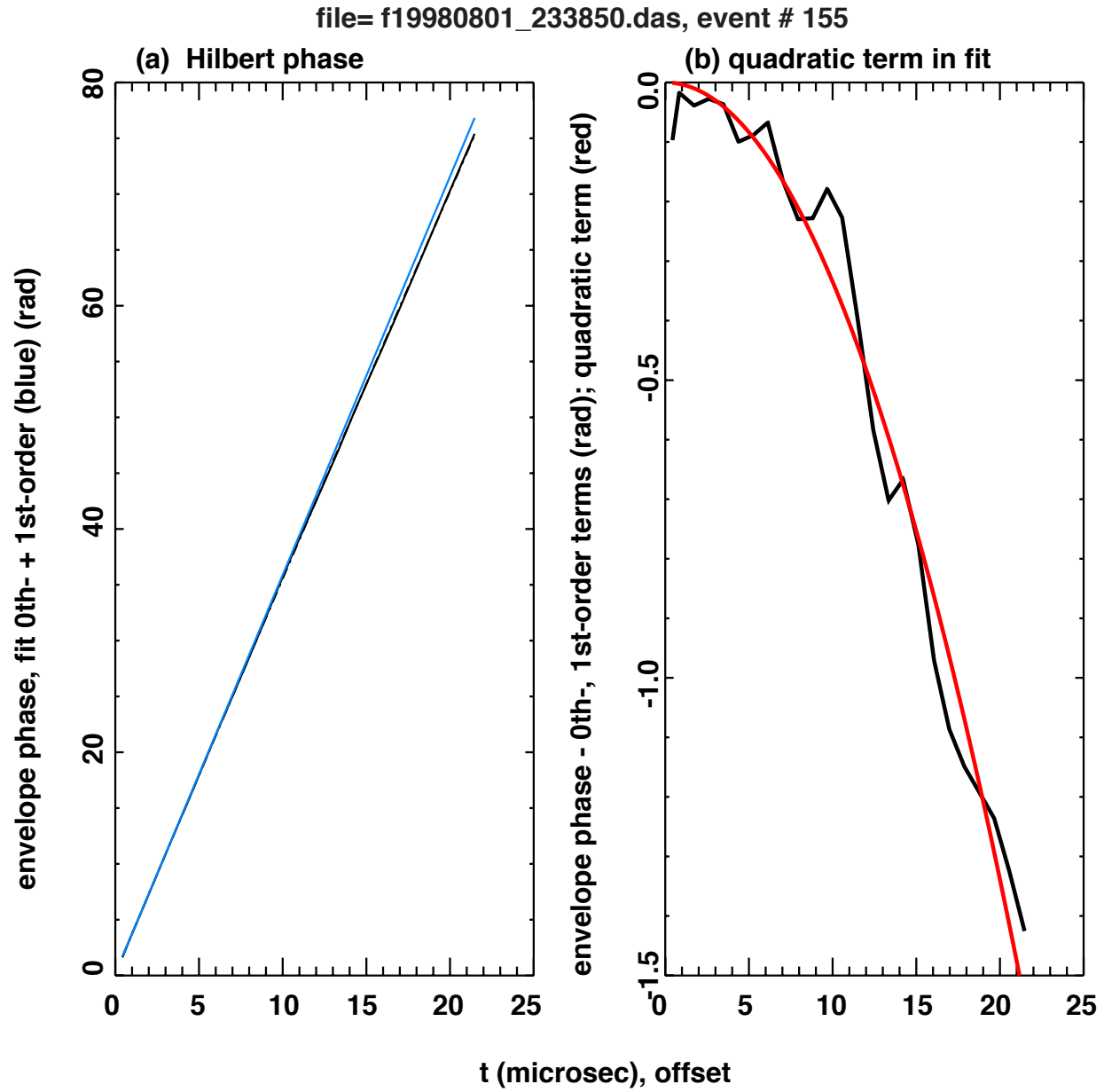
file= f19980801_233850.das, event # 155

Figure 12: Phase of Hilbert envelope vs time. (a) Black: data. Blue: straight-line portion of second-order fit. (b) Black: Residual between data and straight-line portion of second-order fit. Red: Parabolic portion of second-order fit.
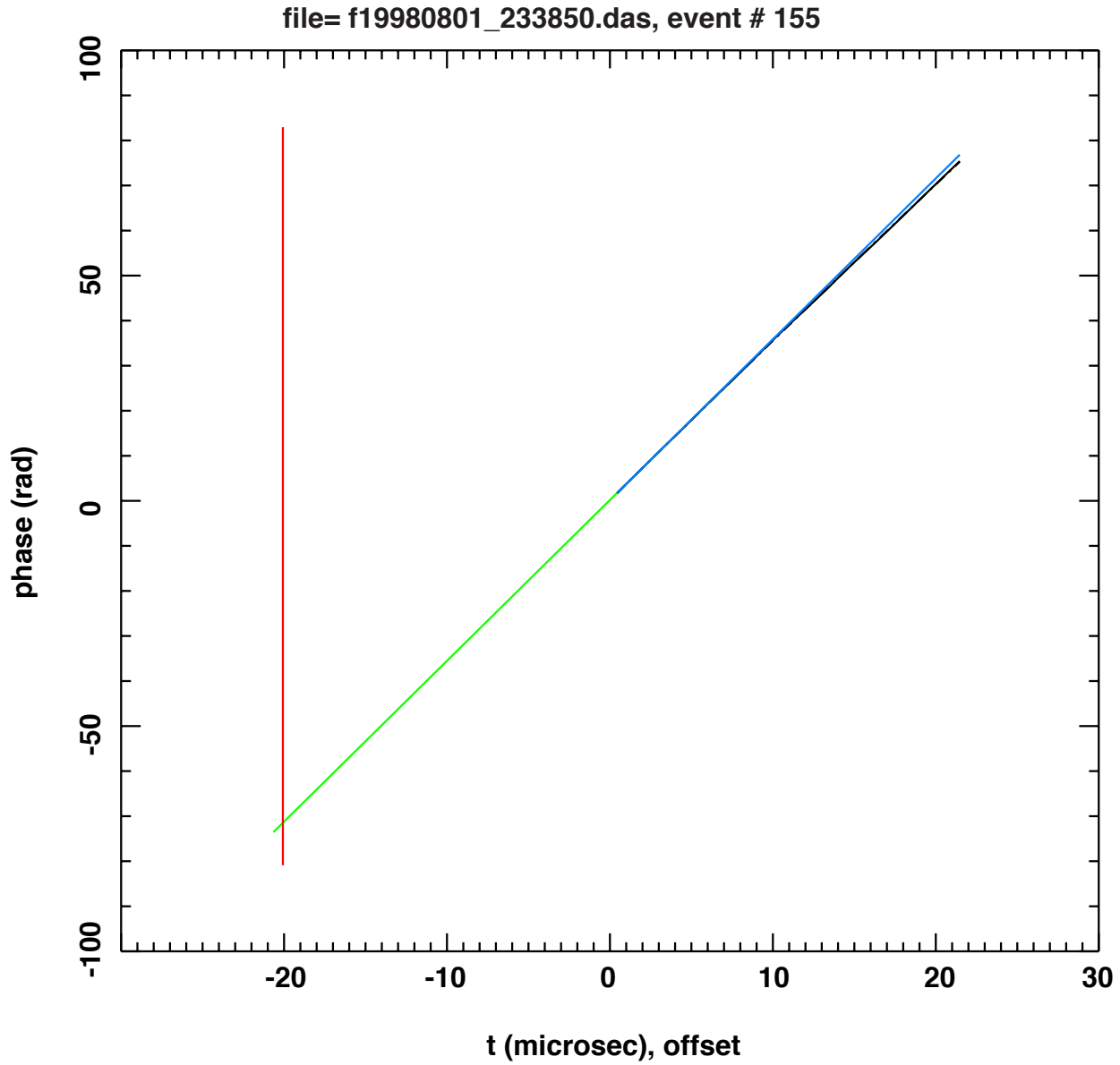
Figure 13: Hilbert-envelope phase vs time. Green: Extrapolation of straight line back to red line. Black: data. Blue: Straight-line portion of 2nd-order polynomial fit of data. Red: Time of arrival at infinite frequency.
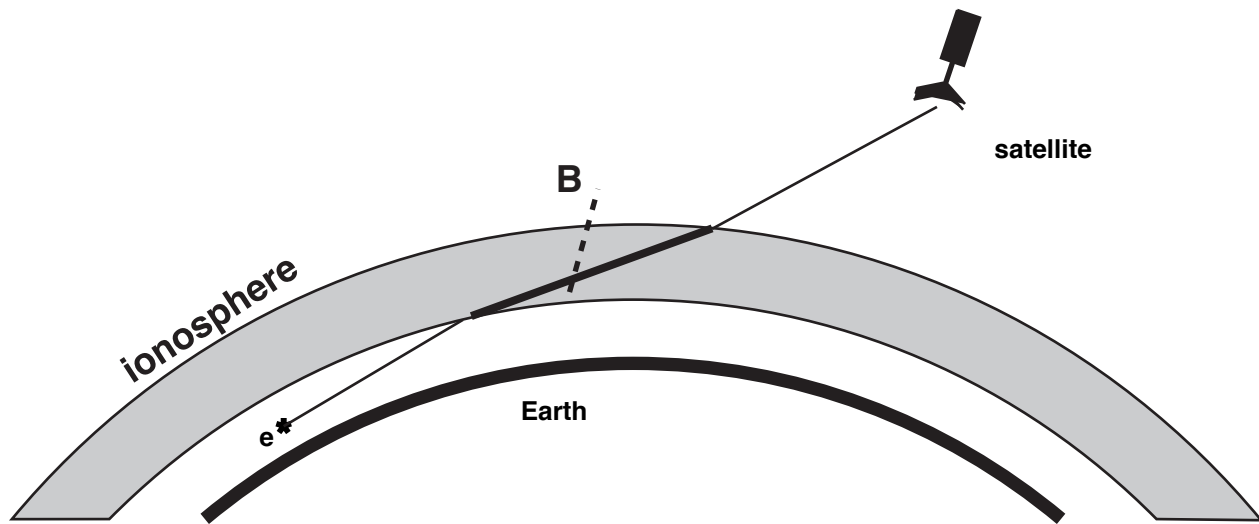
Figure 14: Cartoon of raybending for transionospheric radio path. This treats the case (which is true for our example) of the raypath less inclined than the geomagnetic field.

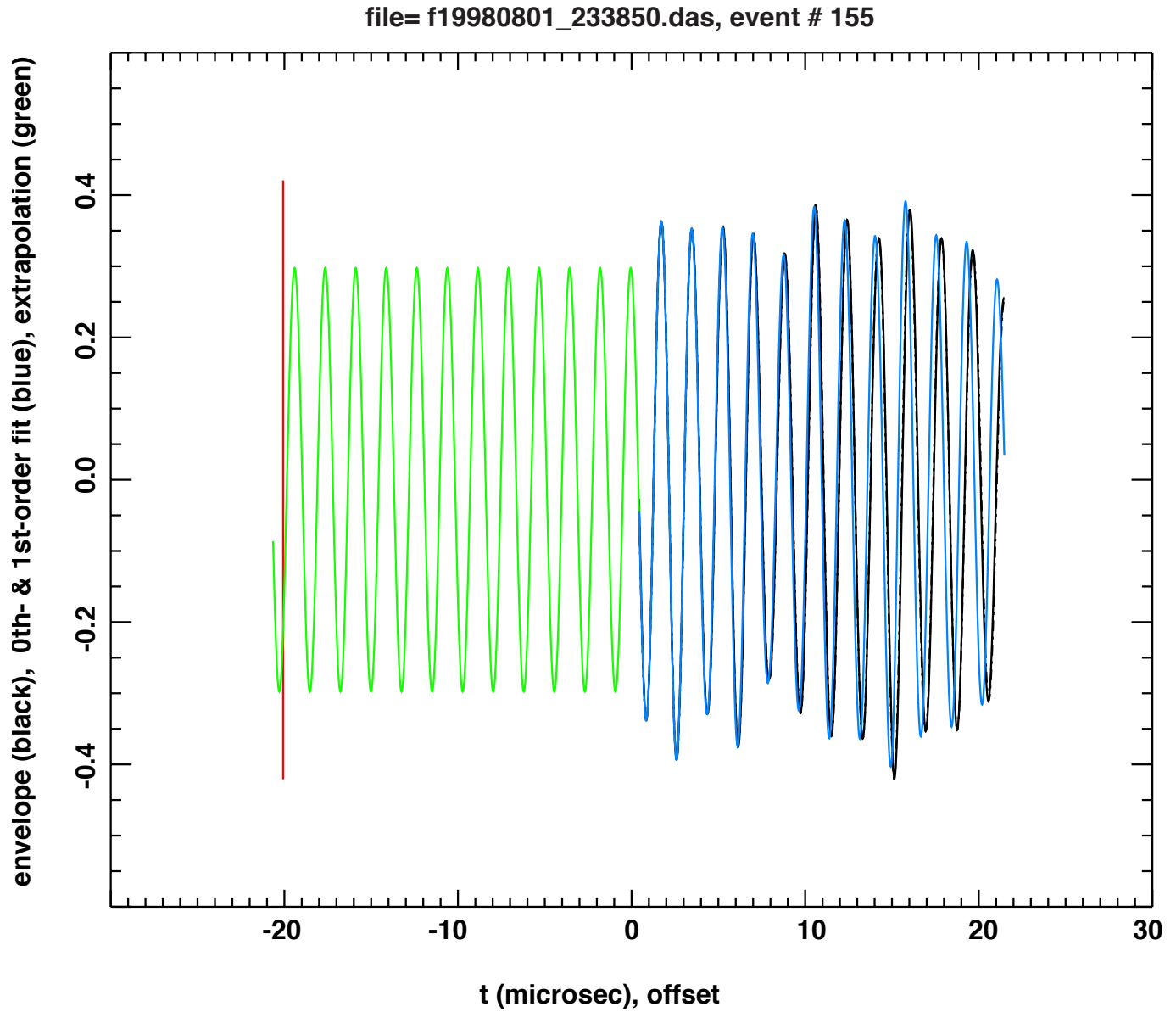**file= f19980801_233850.das, event # 155**

Figure 15: Hilbert envelope. Green: extrapolated back to red line. Black: data. Blue: model using observed amplitude and phase given by straight-line portion of 2nd-order polynomial fit of data. Red: Time of arrival at infinite frequency.
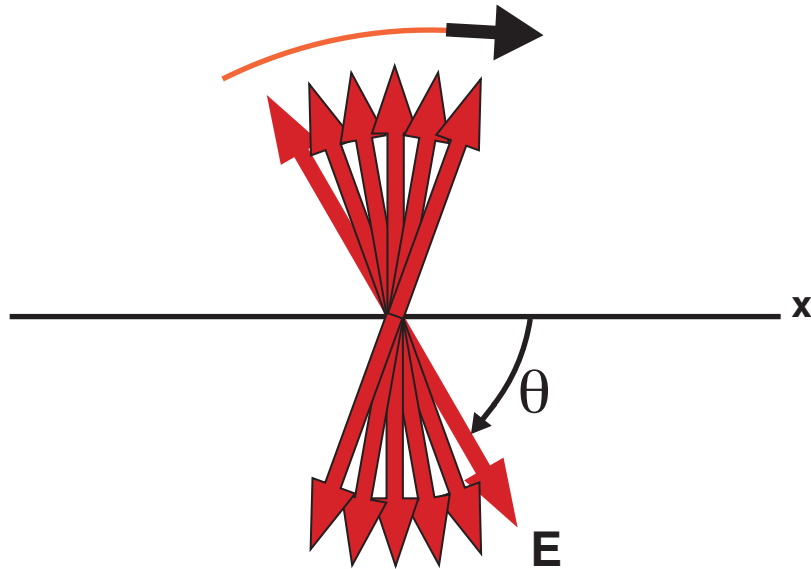
Figure 16: Cartoon of electric field undergoing regular precession in the plane normal to nadir and containing a single antenna. Goniometry with only one antenna may be possible if the angular rate of electric-field precession can be measured and if there is an accurate estimate of the time of arrival for the infinite-frequency limit.